



**HAL**  
open science

## CFD analysis of the flow pattern and local shear rate in a scraped surface heat exchanger

Mourad Yataghene, Jérémy Pruvost, Francine Fayolle, Jack M Legrand

### ► To cite this version:

Mourad Yataghene, Jérémy Pruvost, Francine Fayolle, Jack M Legrand. CFD analysis of the flow pattern and local shear rate in a scraped surface heat exchanger. *Chemical Engineering and Processing: Process Intensification*, 2008, 47 (9-10), pp.1550-1561. 10.1016/j.cep.2007.07.009 . hal-02534072

**HAL Id: hal-02534072**

**<https://hal.science/hal-02534072>**

Submitted on 15 Sep 2023

**HAL** is a multi-disciplinary open access archive for the deposit and dissemination of scientific research documents, whether they are published or not. The documents may come from teaching and research institutions in France or abroad, or from public or private research centers.

L'archive ouverte pluridisciplinaire **HAL**, est destinée au dépôt et à la diffusion de documents scientifiques de niveau recherche, publiés ou non, émanant des établissements d'enseignement et de recherche français ou étrangers, des laboratoires publics ou privés.

# CFD analysis of the flow pattern and local shear rate in a scraped surface heat exchanger

Mourad Yataghene a, Jérémy Pruvost b, Francine Fayolle a, Jack Legrand b

a Ecole Nationale d'Ingénieurs des Techniques des Industries Agricoles et Alimentaires, Département Génie des Procédés Alimentaires, Rue de la Géraudière, GEPEA – UMR CNRS 6144, BP 82225, 44322 Nantes, Cedex 3, France  
b Université de Nantes, GEPEA – UMR CNRS 6144, CRTT-BP 406, 44602 Saint Nazaire, Cedex, France

## Abstract

A numerical investigation of a scraped surface heat exchanger (SSHE) was undertaken using the commercial CFD code FLUENT to characterize the shear rates for Newtonian and Non-Newtonian fluids. Simulations are carried out in standard geometries of SSHE. The electrochemical method was first employed to achieve experimental measurements of the shear rates. A two-dimensional model was created to perform the simulation, keeping the dimensions and flow parameters of the experiment. Because of the symmetry of the geometry, a bidimensional resolution of the continuity and momentum equations was conducted. A hybrid mesh was retained with a grid refinement between the tip of the blades and stator where high shear rates occur. A single reference frame approach was then applied to obtain the laminar steady-state flow induced by the rotation of blades in the geometry. A grid refinement in the zone localized between the tip of the blades and the stator is used. A comparison of predictions with experimental measurements was carried out, showing relative agreement between shear rates ( $S_{\max}$ ) predicted and measured for three fluids (HV45, CMC and guar gum). The little differences observed were principally explained by the 2D simulation which neglects Taylor vortices, when Taylor number ( $Ta_g$ ) exceeds a critical value. In the case of HV45, rotating velocity can influence the scraper angle position due to the floating blade. This can induce a change in the gap between the tip of the blade and stator assembly (from 90 to 130  $\mu\text{m}$ ) that was investigated here.

*Keywords:* Scraped surface heat exchanger; Shear rate; Non-Newtonian fluid; CFD; Mixing; Simulation

## 1. Introduction

Scraped surface heat exchangers (SSHE) are used in the food industry for heating or cooling viscous liquids, liquid–solid suspensions, multiphase fluid systems and for crystallization process [1–3]. These products have a strong viscosity, which poses a problem of clogging on the walls inside the exchanger. SSHEs consist of an external cylinder (stator) which is the heat exchanger surface with the fluid, and an internal cylinder (rotor), concentric or eccentric. The rotor is equipped with the scraping blades, which can rotate. The fluid flows in the annular space

between the two cylinders, while the external surface is constantly scraped; an axial flow is imposed at the inlet of the exchanger using a volumetric pump at a given flow rate (Fig. 1).

The basic flow behaviour in SSHEs, introduced by Trommelen and Beek [4], is a superposition of a rotational velocity (Couette-type) due to the rotation of the inner cylinder and of an axial flow (Poiseuille-type). The flow pattern in SSHEs is complex, and experimental investigations are very difficult to handle as well as to analyse. Therefore, few experimental studies can be found in literature (De Goede and De Jong [5], Dumont [6], Härröd [2], and Maingonnat and Corrieu [7], . . .). Moreover, it is very difficult to treat both hydrodynamics and thermal studies in such a complex geometry. Experimental studies are either focusing on flow behaviour [4–6] in isothermal conditions, or on thermal treatment regardless of the flow pattern [3,7]. Using the electrochemical technique described by Legrand and Coeuret [8], shear rates in SSHEs have been measured successfully by Dumont et al. [9,10] and Mabit et al. [11]. This technique has

*Abbreviations:* SSHE, scraped surface heat exchanger; CFD, computational fluid dynamics; FVM, finite volume method; FEM, finite element method; FDM, finite difference method; 2D, two-dimensional geometry; CMC, carboxymethylcellulose; SM, sliding mesh; MRF, multiple reference frames

\* Corresponding author. Tel.: +33 2 51 78 54 80; fax: +33 2 51 78 54 67.

*E-mail address:* fayolle@enitaa-nantes.fr (F. Fayolle).

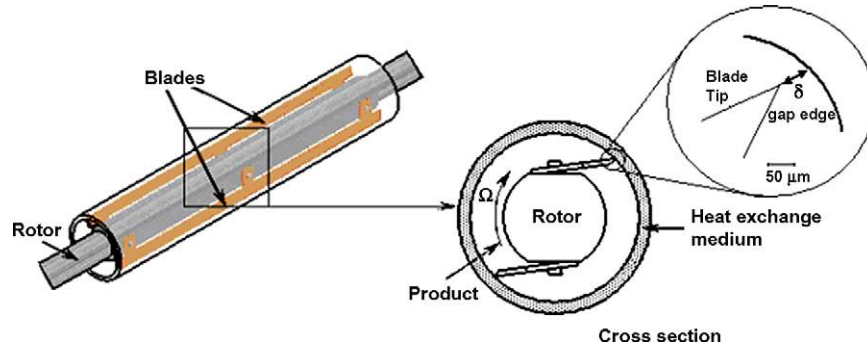


Fig. 1. Schematic representation of: (left) isometric SSHE, (right) cross-section with gap between the tip of the blade region and the stator surface.

allowed the determination of shear rates at the wall. A high increase of shear rate was observed when an electrochemical probe was scraped by one of the blades. Many different studies have been done in order to find models representing the flow behaviour in SSHEs [12–15]. These models express strain rate with respect to the SSHE parameters such as axial flow, number of scraping blades, rotating speed and geometry. However, only the one proposed by Trommelen et al. [16] can predict high shear rates located between the edges of the blades and the outer wall surface.

The progressive increase of rotating speed generates hydrodynamic instabilities known as Taylor instabilities: near a critical value of Taylor number, the flow changes from pure laminar to vortex, wavy vortex, and helicoids vortex flow up to turbulence regime. Härröd [2] indicated that the transition between laminar and vortex regime is very hard to predict accurately in SSHEs with visual methods. Dumont et al. [9,10] confirmed that the transition between laminar and vortex flow regime is not really defined: by using visualization methods they determined a value of generalized Taylor number when vortices appear around  $Ta_g \approx 80$ . Another important parameter introduced by Trommelen et al. [16] is the clearance between the edge of the blades and the stator wall which influences shear rates; this parameter will be used in this study.

Because of the low axial flow rate compared to rotational speed in industrial conditions, the problems can be reduced to 2D geometry. Therefore, numerical simulations in SSHEs were undertaken by several authors, mostly in 2D cross-section geometry [3,5,17–20]. Another approach is to consider a simpler geometry (for example a lid-driven cavity, Sun et al. [21]), in three dimensions. According to these authors, flow behaviour obtained in these geometries can then be used to interpret the behaviour obtained in more complex geometries such as SSHEs, especially with shear-thinning fluids submitted to high shear rates.

The objective of all these works is to resolve hydrodynamic and heat transfer equations in SSHEs while varying the following parameters: fluid rheology, rotational speed, radius ratio, gap space, flow behaviour (laminar or turbulent regime), number of blades, and heat transfer coefficients. Blades take an important role on flow pattern, hence in the heat transfer as well. When Taylor vortices appear, local wall shear rates in a SSHE are controlled by rotating blades [10]. There are many computational

fluid dynamics (CFD) approaches to discretise the equations of conservation of momentum, mass, and energy coupled with constitutive equations that define the physical properties of the fluid as well as the boundary and initial conditions that govern the flow behaviour. The most widely used approaches are finite difference (FDM), finite volume (FVM), and finite element (FEM). CFD is usually based on finite volume method, the details of the schemes discretisation being given by Patankar [22]. Xia and Sun [23] have made a review of applications in the food industry. Numerical modelling gives complementary information to experimental characterization, when the geometry or/and physical phenomena are complex, which is particularly the case in SSHEs.

The objective of the present work is the characterization of the hydrodynamics inside SSHEs in the laminar regime with viscous Newtonian and non-Newtonian fluids. When experimental measurement exists, it is compared to simulation in order to verify the model reliability. Then, new information given by the model is emphasized and the flow behaviour is explained.

Whereas Wang et al. [20], Stranzinger et al. [18] and Sun et al. [19] consider that the blade is in direct contact with the stator wall, experimental measurements [24] tend to show that there is a gap between the tip of the blade and the outer wall surface. This gap can be estimated knowing the shear rate on the leading edge of the blade using Trommelen’s law [16].

The particularity of this work is to simulate the flow and shear rate in SSHEs with geometry as close as possible to the real experimental or industrial geometry, hence including the influence of the distance between the tip of the blade and stator wall, which was evaluated around  $100 \mu\text{m}$ .

To the best of our knowledge, so far no simulations of SSHEs have been done in 3D, taking into account the “real” geometry of the exchanger, especially the gap between the tip of the blade and the stator. As explained before, a 2D approach of the cross-section of the exchanger should give valuable information with a reasonable computation time.

Forthcoming, we will first summarize the experimental method used to measure the shear rate by Dumont [6] and Mabit [24], then we will describe the numerical model and the way it was validated according to experimental flow patterns and shear rates. To conclude, several computations will be done to obtain flow patterns where measurements cannot be obtained.

The aim of a scarped surface heat exchanger is, namely, to exchange heat. It is clear that the thermal dependence of physical properties, viscosity in particular, will play an important role in the flow behaviour. However, experimental results for shear rates can only be obtained in isothermal conditions. This paper aims to compare simulation with existing experimental results in a first approach. Then, the numerical model may be completed in order to take thermal aspects into account. This will be dealt with forthcoming papers.

## 2. Summary of experimental investigation

Determination of shear rates was performed in our laboratory by Dumont [6], and Mabit [24] in previous studies, using electrochemical probes. The electrochemical apparatus and equation derivations are detailed by Dumont et al. [9] and will only be summarized here.

The principle consists in measuring the electrical current  $I$  delivered by a platinum microelectrode which results from a very fast redox reaction:  $\text{Fe}(\text{CN}_6)^{3-} + e^- \leftrightarrow \text{Fe}(\text{CN}_6)^{4-}$  with a large excess of supporting electrolyte  $\text{K}_2\text{SO}_4$ , so as to eliminate the migration current due to the electric field. A voltage difference  $\Delta V$  is set between the probe (the working electrode) and a large counter electrode (the shaft). If  $\Delta V$  is large enough on the microelectrode, the concentration of the reacting ion tends to zero and the current reaches a limit value  $I$ . This limiting current is fully controlled by diffusion only. If the flow fluctuations are slow enough, the quasi-steady relation can be applied to relate the wall shear rate,  $S$ , to the limiting diffusion current,  $I$  [25]:

$$S(t) = \left( \frac{1.477}{zF} \right) \frac{I(t)^3}{D^2 C_0^3 d^5} \quad (1)$$

where  $z$  is the number of electrons involved in the redox reaction,  $F$  the Faraday constant,  $d$  the diameter of the circular microelectrode,  $C_0$  the bulk concentration of the active ions and  $D$  is the diffusion coefficient of these ions in solution.

Table 1  
Geometrical characteristics of the experimental SSHE

Stator diameter ( $d_s$ ) (m)	0.065
Stator length ( $L$ ) (m)	0.38
Ratio ( $L/d_s$ )	5.85
Rotor diameter ( $d_r$ ) (m)	0.04
Exchange surface ( $\text{m}^2$ )	0.0776

However, Eq. (1) can only be used for signals which do not present large variations of diffusion current because it supposes a quasi-steady mode. For fast variation of the diffusion current, the unsteady term has to be taken into account. Sobolik et al. [26] proposed an expression for this case given by the following equation:

$$S_c(t) = S(t) + \frac{2}{3}t_0 \left( \frac{\partial S}{\partial t} \right) \quad (2)$$

where  $S_c(t)$  is the value of the shear rate corrected with respect to the probe inertia.

$S_c(t)$  values calculated with Eq. (2) will be compared with numerical results.

## 3. Description of numerical method

### 3.1. Geometry and meshing

The geometry of the computational model has been created using Gambit<sup>®</sup> software (Fluent.Inc). Dimensions and scraper angle of the experimental set-up used by Dumont [6] were used. A schematic representation is given in Fig. 1, with dimensions in Table 1. If the axial flow is neglected, SSHE simulation can be reduced to 2D cross-section with two blades. An important feature when discretising the computational domain is to have a sufficient refinement along the direction of velocity gradient, namely around blades in our case. The resulting grid is shown in Fig. 2. Due to the blades, and especially to the thin gap between the tip of the blade and the stator wall which is around  $100 \mu\text{m}$ , a

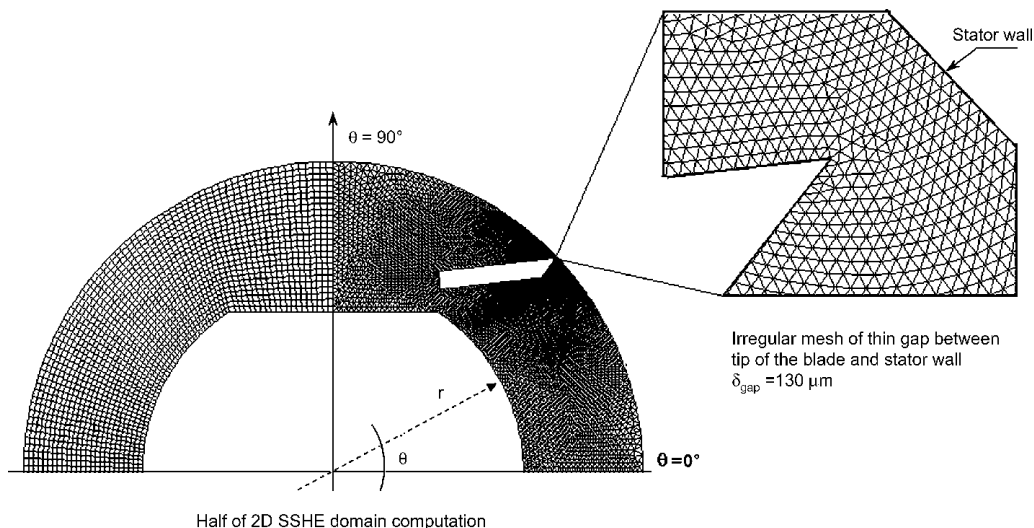


Fig. 2. Mesh topology of 2D SSHE.

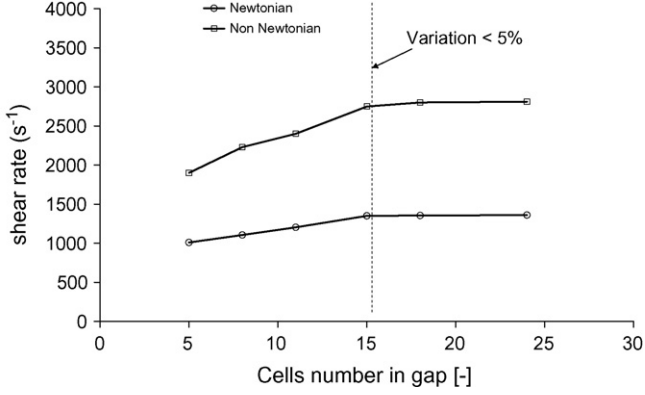


Fig. 3. Grid independency and selection of the mesh.

structured grid is difficult to apply in the entire geometry. Therefore, a hybrid mesh was retained with an irregular part consisting in triangular elements in the blade zone, the remaining fluid domain being regularly meshed with quadrilateral elements. In the gap zone between blade tip and stator, a particular attention was paid to the mesh refinement (Fig. 2).

Grid independence is an important stage in CFD modelling: it is necessary to check that the influence of the additional grid near the tip of the blade does not change the calculation of the maximum shear rate at the stator wall for Newtonian and non-Newtonian power law fluids as well as the calculation of the apparent viscosity of the power law fluids. Fig. 3 shows the value of  $S_{\max}$  which is the maximum shear rate at the stator wall and is calculated from the velocity field using the magnitude of the strain tensor (Eq. (3)).

$$\dot{\gamma} = \frac{1}{2}[\text{grad}\vec{v} + \text{grad}\vec{v}^T] \quad (3)$$

Fig. 3 shows that, if the number of cells in the thin gap is not sufficient, the numerical computation of the velocity gradient varies with the number of cells. Meanwhile, when this number reaches a certain limit, it can cause numerical diffusion of the solution, which can induce an error in the numerical computation. As shown in Fig. 3, the maximum shear rate calculated at the stator surface for Newtonian fluid (HV45 35%,  $N=1$  rps) becomes constant when the number of cells in the gap reaches 18, respectively, 24 for non-Newtonian fluid. However, when using the grid with 15 cells, the relative error calculated by considering the stabilization criterion at 24 cells is lower than 5%, for both Newtonian and non-Newtonian fluids. In order to reduce the computational time, we decided that 5% was an acceptable error, and the grid refinement with 15 cells was chosen for the entire study.

### 3.2. Governing equation and numerical method

Fluent software is based on FVM method to solve momentum and convection–diffusion equations. The flow is laminar and isothermal. Rotation of the blades is solved using single reference frame. In this case, governing equations (continuity and momentum equations) have to be expressed in the rotating reference frame. In most expected applications of the SSHE, shear rates induced by axial flow are negligible compared to the very

strong local shear rates due to the circumferential velocity of the rotor and the blades. Consequently a simulation of a 2D cross-section of the SSHE seems reasonable. The Taylor number is one of the important dimensionless numbers used in SSHE; it is based on the angular velocity. If the Taylor number exceeds a critical value ( $Ta_c$ ), the instability caused by curved streamlines on the main flow produces asymmetric Taylor vortices and can influence shear rates. There are two definitions of the Taylor number: Eq. (4) in the case of Newtonian fluid, and Eq. (5) for the generalized Taylor number used in the case of non-Newtonian fluids (using power law model as flow behaviour model).

$$Ta = \frac{\rho R_r (R_s - R_r)}{\eta} \left( \frac{R_s - R_r}{R_r} \right)^{1/2} \Omega \quad (4)$$

$$Ta_g = \frac{\rho d_h^n}{2^n} \left( \frac{R_s - R_r}{R_r} \right)^{1/2} \frac{(\Omega R_r)^{2-n}}{k} \quad (5)$$

In industrial SSHEs, Taylor numbers are generally comprised between  $0 < Ta_g < 100$ , which corresponds to rotating velocities  $N$  from 0 to 10 rps. In the geometry used for our investigation, Taylor numbers do not exceed 80. This value, as observed by Dumont [6], corresponds to the Taylor vortices appearance. In a first assumption, Taylor vortices can then be neglected in our operating conditions.

Conservation of momentum equation is described by

$$\frac{\partial}{\partial t}(\rho \vec{v}) + \nabla \cdot (\rho \vec{v} \vec{v}) = -\nabla p + \nabla \cdot (\vec{\tau}) + \rho \vec{g} + \vec{F} \quad (6)$$

where  $p$  is the static pressure and  $\rho \vec{g}$  and  $\vec{F}$  are gravitational body force and external forces and  $\vec{\tau}$  is the stress tensor.

The rotation axis is parallel to the  $z$ -axis, and the relative velocity is given by:

$$\vec{v}_r = \vec{v} - (\vec{\Omega} \times \vec{r}) \quad (7)$$

where  $\vec{\Omega} \times \vec{r}$  is the angular velocity vector, and  $r$  the position vector in rotating frame. In the rotating reference frame, the continuity equation becomes:

$$\frac{\partial \rho}{\partial t} + \nabla \cdot (\rho \vec{v}_r) = 0 \quad (8)$$

where  $v_r$  is the relative velocity vector in the rotating frame.

In terms of relative velocities the left hand side of Eq. (6) can be written as:

$$\frac{\partial}{\partial t}(\rho \vec{v}_r) + \nabla \cdot (\rho \vec{v}_r \vec{v}_r) + \rho(2\vec{\Omega} \times \vec{v}_r + \vec{\Omega} \times \vec{\Omega} \times \vec{r}) + \rho \frac{\partial \vec{\Omega}}{\partial t} \times \vec{r} \quad (9)$$

The third term in Eq. (9) is the Coriolis force. In the reference frame method, Eqs. (8) and (9) are solved for a given value of  $\Omega$  (rotating speed of the blades). The absolute velocity is then obtained using Eq. (7).

### 3.3. Rheological model

Fluids processed in SSHEs are generally non-Newtonian; where the viscosity  $\eta$  is a non-linear function of the shear rate  $\dot{\gamma}$ .

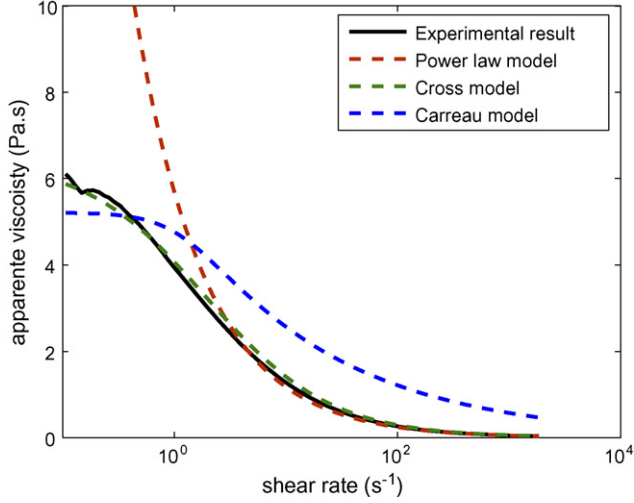


Fig. 4. Rheological behaviour of the guar gum 0.8% at 20 °C and models comparison.

Several mathematical models are available to describe the rheological behaviour of a fluid. Because of the closure problem of the momentum equation in the case of non-Newtonian fluids, it is necessary to describe the rheological behaviour with a mathematical model.

Stranzinger et al. [18], used Carreau–Yasuda model which introduces numerical limits to viscosity, which gives a better performance in the transition regions of viscosity curves and describes both upper and lower viscosity plateaus: at a very strong shear rate, the value of apparent viscosity is  $\eta_\infty$  and at zero shear rate  $\eta_0$ .

In the present study, two types of models were used: cross model was used for the guar solution. Power law model was chosen to describe CMC solution, with a changed limit conditions at weak and high shearings.

In the case of guar solution, Fig. 4 shows the cross model as well as the power law and Carreau models compared to measurements obtained using a rheometer instrument (AR1000). The more accurate model in this case is the cross model, it was then selected to handle the simulation. For our guar solution, the cross model is described by the following equation:

$$\eta_{app} = \frac{\eta_0}{1 + \lambda \dot{\gamma}^n} \quad (10)$$

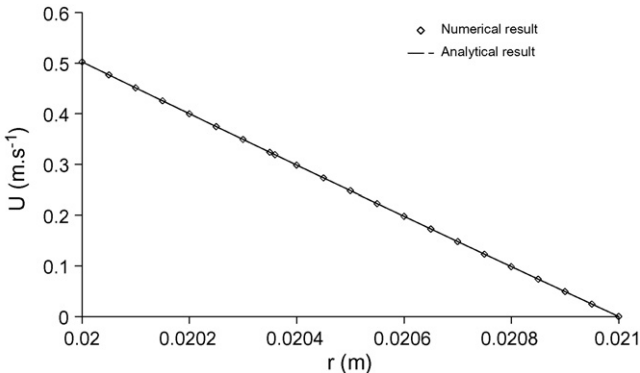


Fig. 5. Numerical and analytical Couette validation in annular gap in case of CMC 1.5% ( $k = 3 \text{ Pa s}^n$ ,  $n = 0.5$ ,  $e = 1 \text{ mm}$ ,  $\Omega = 30 \text{ rad s}^{-1}$ ).

Table 2  
Physical properties of HV45 25 °C

Solution	Water (w/w)	$\rho$ (kg/m <sup>3</sup> )	$\eta$ (Pa s)
HV45	20%	1080	1.18
HV45	35%	1073	0.43

Table 3  
Physical properties of CMC 25 °C (power law model)

Solution	$\rho$ (kg/m <sup>3</sup> )	$k$ (Pa s <sup>n</sup> )	$n$	$\eta_{max}$	$\eta_{min}$
CMC 0.9%	1047	1.98	0.55	2.0	0.01
CMC 1.1%	1048	4.44	0.48	4.5	0.01

with  $\eta_0$  is zero viscosity,  $\lambda$  is time constant, and  $n$  consistency index.

To prevent mathematical problems when solving equations, the power law model chosen for CMC is used with viscosity limits at the low and high shear rates. The final description of the model law is then:

$$\eta_{app} = k \cdot \dot{\gamma}^{n-1} \quad (11)$$

$$\eta_{min} < \eta_{app} = k \cdot \dot{\gamma}^{n-1} < \eta_{max}.$$

$$\text{with limits } \eta_{min} = \lim_{\dot{\gamma} \rightarrow \infty} (\eta_{app}), \quad \eta_{max} = \lim_{\dot{\gamma} \rightarrow 0} (\eta_{app})$$

To validate the choice of the fluid behaviour, series of simulation were done in the case of a Couette flow where the analytical solution for velocity is:

$$V_r = V_z = 0, \quad V_\theta = \Omega \cdot r \left( \frac{r^{-2/n} - r_c^{-2/n}}{r_i^{-2/n} - r_c^{-2/n}} \right) \quad (12)$$

where  $r$ ,  $\theta$ ,  $z$ , represent the radial, azimuthal and axial directions of the cylindrical coordinate system, respectively. The angular velocity of the inner cylinder is denoted  $\Omega$ ; the inner and outer radii are represented by  $r_i$  and  $r_c$ , respectively.

The reliability of the numerical procedure was tested by comparison to analytical results obtained for a Couette cell with 1 mm annular gap. Using the power law model with limits viscosities (i.e. Eq. (11)), the result agrees remarkably well with the analytical solution, as shown in Fig. 5.

Physical properties of the working fluids are summarized in Tables 2–4, respectively, for HV45, CMC and guar gum.

### 3.4. Boundary conditions and numerical details

Flow equations being solved only in a SSHE cross-section, no inlet and outlet flow conditions are applied and the flow is generated mainly by the rotation of the blades. Two approaches can be used to simulate the rotating flow, one based on rotating

Table 4  
Physical properties of guar 25 °C (cross model)

Solution	$\rho$ (kg/m <sup>3</sup> )	$\lambda$ (s)	$n$	$\eta_0$ (Pa s)	$\eta_\infty$ (Pa s)
Guar 0.7%	1046	0.50	0.60	1.02	$1.35 \times 10^{-3}$
Guar 1.0%	1047	0.37	0.75	2.60	$1.00 \times 10^{-2}$

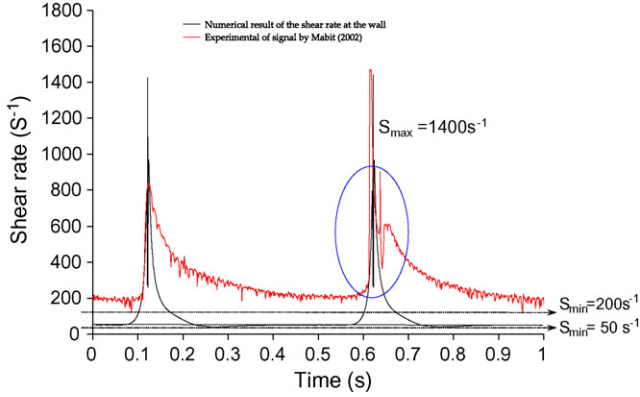


Fig. 6. Comparison between experimental and numerical shear rates at the wall in case of CMC 0.7% with  $N = 1$  rps.

reference frames, and the other one is sliding mesh (SM). As explained before, a single rotating reference frame was applied here, which is the simplest solution. In the SM technique, two or more cells zones are used, a part corresponding to stationary zone, the other ones being associated with rotating parts. The two grids then slide past each other in a time-depending manner. Such resolution is highly time-consuming, because of its unsteady nature. However, the SM approach can model interaction of fluid zones with moving parts efficiently. Such approach would be necessary if the rotor–stator interaction were strong. For the case under study, a resolution based on single reference frame proves sufficient. Corresponding equations are discussed in (Section 3.2). The blades and rotor are considered as moving walls, with angular velocity  $\Omega$ , the stator being immobile. The definitive boundary conditions are:

- At the stator surface  $V = 0$
- On the rotor  $V = \Omega \times r$
- On the blades  $V = \Omega \times r$

where  $\Omega$  is the angular velocity, and  $r$  radial coordinate.

In Fluent software, the governing integral equations for mass and momentum conservation are solved, with a segregated approach where equations are solved sequentially with implicit linearization. Volume-faces advective fluxes are approximated using a second-order upwind interpolation scheme. The pressure–velocity coupling is considered using the iterative correction procedure (Simple algorithm). For all simulations, the solution was considered converged when the total residuals for the continuity and momentum equations is equal to  $10^{-6}$ .

## 4. Results and discussion

### 4.1. Signal comparison

Series of signals obtained by the electrochemical method are analysed. Fig. 6 shows the time evolution of  $S$  obtained at the stator wall ( $r = R_c$ ) in the case of CMC 0.7% with a rotating velocity of 1 rps. If experimental results are considered, the first observation is the difference in peak shape for the passage of

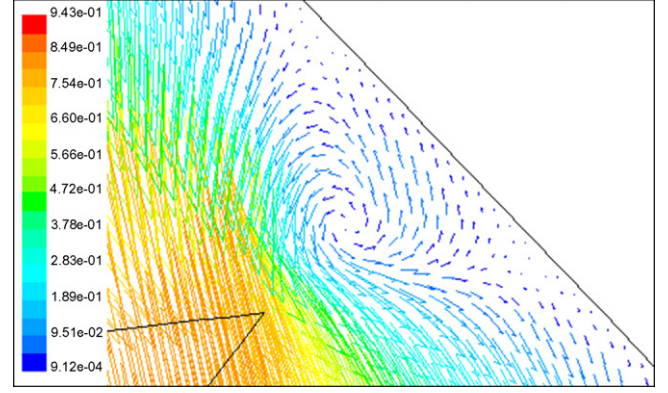


Fig. 7. Velocity field vector between the tip of the blade and the stator wall in case of CMC 0.7%,  $N = 1$  rps.

the two blades. This difference can be explained by the fact that the assembly of the blades is floating, and therefore induces different conditions of scraping for the two blades. The maximum shear rate on the stator wall is obtained with blade 2 ( $\delta_{\text{gap}} = 130 \mu\text{m}$ ). Obviously, because the simulation domain is chosen symmetrically, no difference is observed between both blades in numerical results. Numerical results agree with experimental values of blade 2 of  $S_{\text{max}}$ . However, after the passage of blade 2, the minimum of shear rates ( $S_{\text{min}}$ ) calculated numerically does not agree with experimental results. This difference is mostly due to the presence of the axial flow, which is neglected in the simulation. However, the high speed of the phenomenon which cannot be captured by the frequency acquisition can also explain the difference. The signal obtained experimentally shows a disturbance of the magnitude of the shear rate after the passage of the blade, the signal decreases as expected, and then increases again. This second increase was difficult to explain based only on experiments.

The same configuration is obtained numerically. Moreover, the numerical results give an explanation of the phenomenon. Fig. 7 shows the velocity vectors in the clearance gap, and a recirculation appears in the tip region of the blade.

Fig. 8 gives the numerical magnitude of the shear rate in the clearance space.

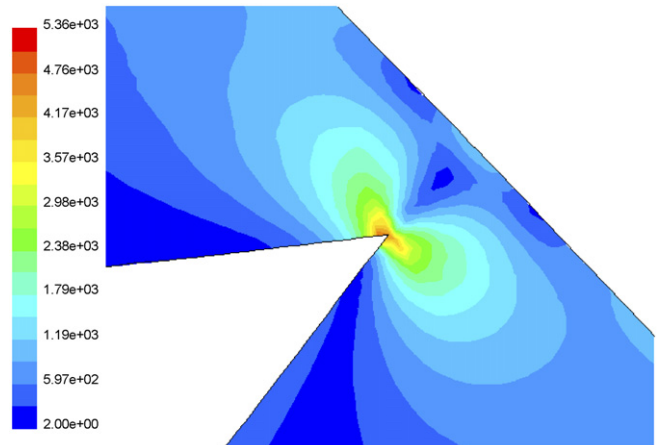


Fig. 8. Magnitude of the shear rate in the clearance space.

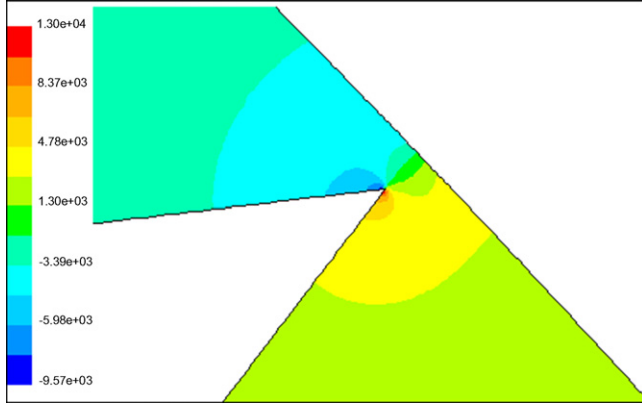


Fig. 9. Pressure distribution in the vicinity of the blade.

Fig. 9 shows the distribution of the pressure in the zone close to the tip of the blade. This figure highlights a depression behind the blade and an overpressure at the front of the blade, which is consistent with velocity fields in this region.

The presence of the recirculation of the fluid in the clearance space is the origin of the disturbance in the shear rate signal obtained experimentally.

Several authors propose models to estimate the average shear rates received by the product in SSHE, principally in annular gap. The various models are given in Table 5.

According to these models, the average shear rates in an annular space do not exceed the value of  $40 \text{ s}^{-1}$  (Table 5). The mean shear rate calculated in the whole computational domain gives the same order of magnitude as those of the models and is  $38 \text{ s}^{-1}$ . This result confirms that the models given in the literature and listed in Table 5 only allow a calculation of the mean shear rates that can be received in a SSHE, but are not suitable for the determination of local shear rates. These local calculations can only be handled by CFD models or local measurements such as the one discussed here.

#### 4.2. Determination of gap width ( $\delta_{\text{gap}}$ )

As explained before, the objective of this simulation is to be as close as possible to the experimental geometry. However, the width of the gap between the tip of the blade and the stator wall cannot be measured precisely, but can only be evaluated thanks to Trommelen and Beek's equation [4]. Moreover, on the experimental set-up, the increase of the rotational speed can lead to a change of  $\delta_{\text{gap}}$  because of the increasing centrifugal forces

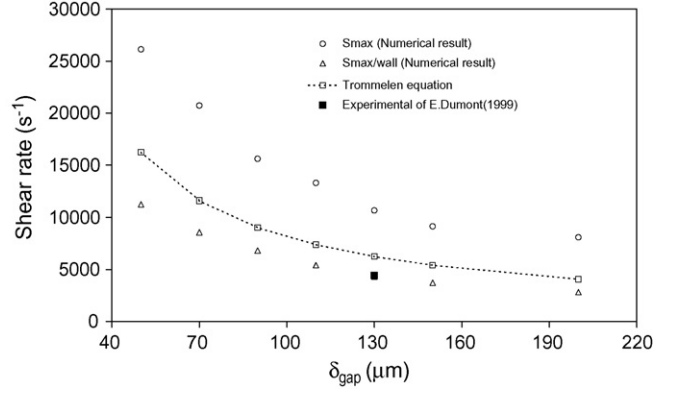


Fig. 10. Comparison between CFD model and Trommelen equation [4], in the case of HV45 20% of water.

and consequently to a change of shear rates. This change of gap is due to the floating assembly of blades in SSHEs. At high rotating speed, shear rates at the wall can reach a very great value, which plays an important role for the mechanical treatment received by the products. As this gap cannot be measured exactly in operating conditions, the value of  $\delta_{\text{gap}}$  was determined so as to obtain experimental value of  $S_{\text{max}}$ .

While experimental results are only given on the exchange surface (stator wall), a numerical approach allows the calculation of the distribution of shear rate magnitude inside the whole computational domain. As displayed in Fig. 8, it can be observed that the maximum shear rate is localized between the blade tip and the stator wall and more precisely near the tip of blades. As explained before, an approximate value of the  $\delta_{\text{gap}}$  was first estimated. The model of Trommelen and Beek [4] was used. Such model gives a correct approximation of the shear rate like other models of literature [12,13,15]. Dumont et al. [10] estimate that  $\delta_{\text{gap}} = 50 \cdot 10^{-6} \text{ m}$  and  $100 \times 10^{-6} \text{ m}$  for Mabit et al. [11]. Fig. 10 shows a comparison of the maximum shear rates at the stator wall and at the tip of blade given by CFD model against the Trommelen model (Eq. (13)) [4]. This model supposes a linear velocity profile in the clearance region. By varying the value of  $\delta_{\text{gap}}$ , the calculations allow an estimation of  $S_{\text{max}}$ , and also permit to set the gap between the tip of the blade and the stator wall.

$$\dot{\gamma}_{\text{max/wall}} = \frac{V_{\text{tip}}}{\delta_{\text{gap}}} = \frac{2\pi R_c N}{\delta_{\text{gap}}} \quad (13)$$

where  $V_{\text{tip}}$  is the blade tip velocity and  $\delta_{\text{gap}}$  is the gap between the tip of blade and stator wall.

Table 5  
Models of shear rates proposed in literature

Authors	Models	CMC 0.7% calculation
Leuliet et al. [13]	(14) $\dot{\gamma} = 3.213 \times 10^4 \times 1.45^{nL} n^{-0.7115} Q + 23.44 Q^{-0.03} n^{0.1754} N$	$\dot{\gamma} = 33 \text{ s}^{-1}$
Maingonnat et al. [14]	(15) $\dot{\gamma} = \xi 1.3^{nL} Q + \beta N$	$\dot{\gamma} = 38 \text{ s}^{-1}$
Naimi [15]	(16) $\dot{\gamma} = \frac{2\sqrt{U_d^2 + (2\pi R_c N)^2}}{d_h}$	$\dot{\gamma} = 32 \text{ s}^{-1}$
Härröd [12]	(17) $\dot{\gamma} = \frac{d_s^2 + d_f^2}{d_s^2 - d_f^2} (2\pi N)$	$\dot{\gamma} = 14 \text{ s}^{-1}$

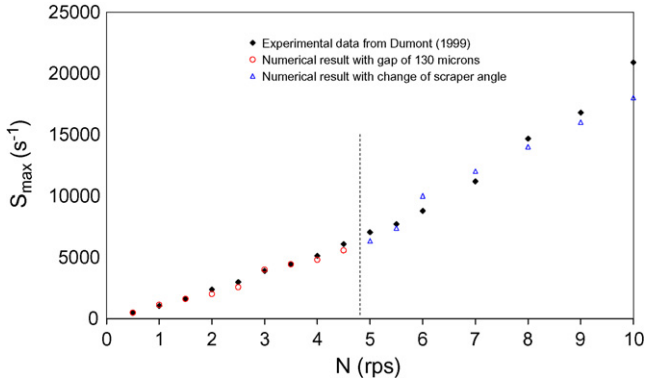


Fig. 11. Numerical and experimental results (Dumont [6]) for  $S_{max}$  in case of (HV45 35% of water).

As shown in Fig. 10, Eq. (13) gives an approximate idea of the maximum shear rate on the stator wall compared with the numerical model as well as the experimental results. It can be noticed that the model proposed by Trommelen and Beek [4] is the only one acceptable for estimated local shear rate at the stator wall. The numerical result shows that the maximum shear rate is not localized in the stator wall, but in the region close to the tip of the blade (Fig. 8). According to this study, the maximum shear rate is generally three to six times higher than  $S_{max}$  at the stator wall, depending on the using fluids.

## 5. Simulation of the flow behaviour for different types of fluids

### 5.1. Newtonian fluid (HV45)

When starting the experimental procedure, the velocity of the rotor which drives the blades is null, and the blades are parallel to the rotor. When the rotor begins to turn, and because of the floating assembly of the blades, the existence of imbalance between the viscous and centrifugal forces can cause a change in the scraping angle of the blades, which is directly related to the gap ( $\delta$ ). Experimental results show a parabolic variation of shear rate with respect of rotating velocity. It is known that the evolution of centrifugal forces by unit of mass ( $F$ ) are proportional to  $N^2$ . This evolution is similar to the one obtained for experimen-

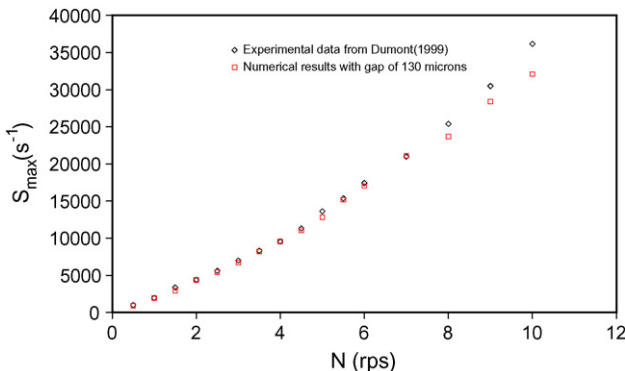


Fig. 12. Numerical and experimental results (Dumont [6]) for  $S_{max}$  in case of CMC 0.9%.

tal shear rates represented in Fig. 11. The main difficulty in the numerical prediction of the flow in industrial SSHEs is to set the gap between the blade and the stator wall. In industrial SSHEs, the gap decreases with the rotational speed which contributes to dramatically increase the shear rate, then the treatment conditions of the product are different. However, a good prediction is obtained by setting two different values of the gap for rotation speed below 5 rps and above the same value. Although it is known that the gap decreases in a constant manner, we chose to keep only two different values corresponding to the two slopes identified further.

The numerical results obtained for HV45 with 35% water were compared with experimental results and shown in Fig. 11. The local shear rate ( $S_{max}$ ) constantly increases with the rotating velocity and is proportional to  $\delta_{gap1} = 130 \mu m$  for rotating speed below 5 rps. As said before, although the gap varies in a constant manner with the increasing rotating velocity, the gap width was changed artificially for 5 rps. For higher values of  $N$  the numerical results are in perfect agreement when using  $\delta_{gap2} = 90 \mu m$ .

### 5.2. Non-Newtonian fluid

#### 5.2.1. CMC (carboxymethylcellulose)

The power law fluid model with limit conditions (see Section 3.3) was used to simulate CMC. At low and high shear rates, the values of apparent viscosities are fixed. The numerical results were compared with experimental investigations handled by Dumont [6] in the case of a 0.9% CMC solution. Fig. 12 gives a comparison between experimental and numerical values of  $S_{max}$ . There is a good agreement between numerical and experimental of maximum shear rates at the wall.

Because of the shear-thinning behaviour of CMC, apparent viscosity at the wall decreases dramatically with increasing rotating velocity. Thus, viscous forces observed previously for HV45 do not exist in this case, so the gap does not change and takes a constant value of  $130 \mu m$ .

#### 5.2.2. Guar gum

As explained before in the case of guar gum the most correct model to describe rheological behaviour is the cross model and

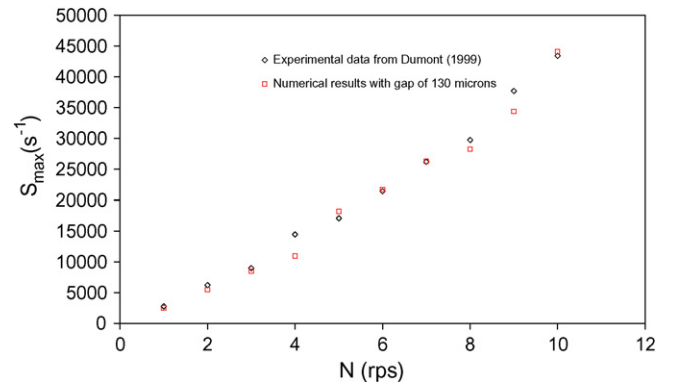


Fig. 13. Numerical and experimental results (Dumont [6]) for  $S_{max}$  in case of guar gum 0.7%.

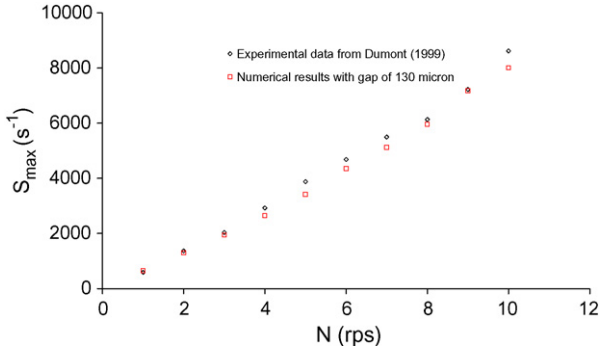


Fig. 14. Numerical and experimental results (Dumont [6]) for  $S_{\max}$  in case of guar gum 1%.

the apparent viscosity is given by Eq. (10). In this simulation, the gap between the tip of the blade and stator wall is fixed at  $130 \mu\text{m}$  for guar 0.7%, and for guar 1%. The experimental results of maximum shear rate obtained with the CFD model were compared with Dumont's data [6].

Figs. 13 and 14 show the shear rates versus the rotational speed for experimental results and CFD model validation. The model gives a good agreement compared with experimental results. In Fig. 13, a slight deviation between the numerical and experimental results can be seen after  $N=7$  rps, corresponding to  $Ta_{cr}=66$ . For the guar 0.7% solution, the value of generalized Taylor number exceeds the critical value of the  $Ta_{cr}=80$  as defined by Dumont [6]. After this value, the Taylor instabilities start, which is not taken into account by the 2D model, and which consequently modifies shear rate and explains the difference. This phenomenon does not occur for 1% guar because of the higher viscosity of the solution.

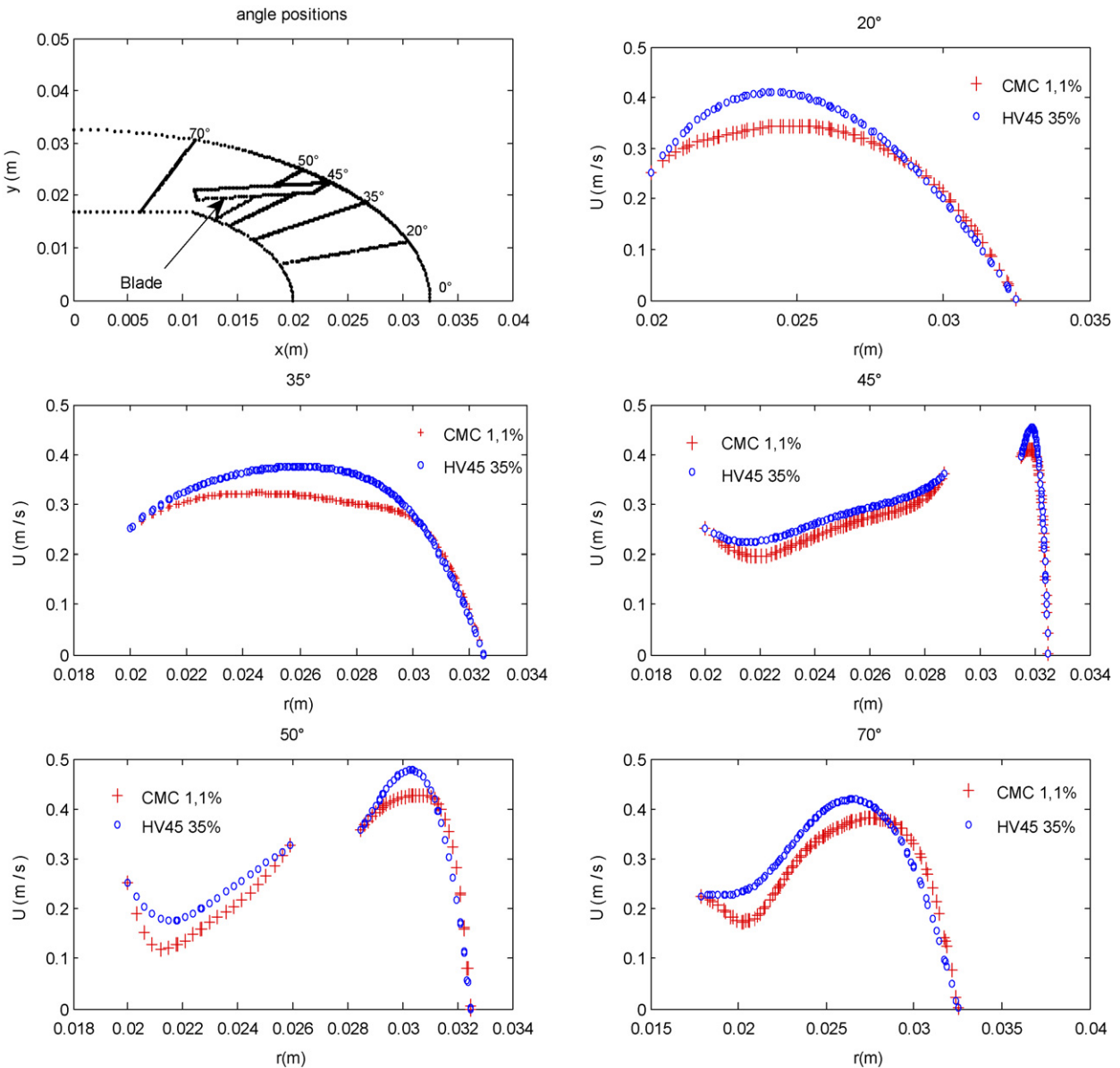


Fig. 15. Calculated velocity for different angle position.

### 5.3. Velocity analysis

As shown before, calculated shear rates are in good accordance with experimental results. However, flow pattern is the key to understand the mixing and heat transfer mechanisms in SSHE. Therefore, the model which can predict the velocity in the whole computational domain is an important tool, which can give non-measurable information. Fig. 15 illustrates the variation of the velocity magnitude versus the radial position at different angle positions ( $20^\circ$ ,  $35^\circ$ ,  $50^\circ$  and  $70^\circ$ ), for a rotating velocity  $\Omega = 4$  rps, and for Newtonian HV45 20% water and non-Newtonian CMC 1.1%. The velocity profiles around the scraper blade is complex, and shows asymmetric parabolic profiles, which indicates superposition of pure pressure driven flow (due to the rotation of scraper blades) and shear-driven flow (due to rotating blades and to the rotation of the inner cylinder). For all angular positions, the difference between Newtonian and non-Newtonian fluids is due to the non-linearity of the viscosity with respect to shear rate: the velocity profiles are more complex for non-Newtonian fluids and highly depend on the flow index behaviour in as mentioned by Wang et al. [20].

### 6. Non-Newtonian viscosity distribution in SSHE

Fig. 16 shows numerical result of the distribution of the apparent viscosity in the SSHE, in the case of a non-Newtonian fluid (CMC 0.7%). The apparent viscosity of the product changes with respect to the shear rate, and is strongly heterogeneous in the SSHE: the stronger shear rates are localized mainly in the space between the tip of the blade and the stator wall, and with a highly shear-thinning product such as CMC, the value of the apparent viscosity in that region can be very weak compared with the overall product. This flow heterogeneity was observed by Mabit et al. [11] by injecting a coloured liquid as tracer, in the case of CMC. A channelling flow where a part of the product moves with a higher speed than in the remainder of the exchanger was visualized. This zone is mainly localized in the space between the blade and the stator wall, where the shear rates are very important compared with the remainder of the exchanger. Fayolle et al. [27] considered that two layers of the fluids must coexist: one layer with very low viscosity close to

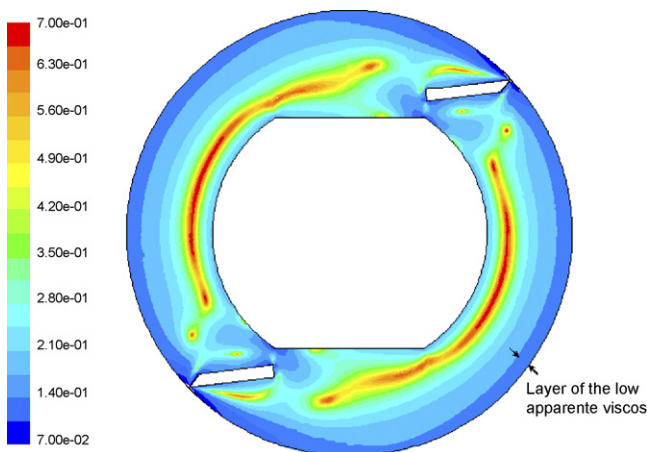


Fig. 16. Distribution field of apparent viscosity in SSHE [CMC 0.7%,  $N = 1$  rps].

the wall, and another one with higher viscosity near the rotor, and that these two layers behave like two immiscible fluids. Numerical results shown in Fig. 16 confirm this hypothesis. In this case, the apparent viscosity of the product is reduced ten times or more; this heterogeneity of the apparent viscosity gives a separation of the fluid which can move with different speeds.

### 7. Conclusion

CFD was used in order to predict the local shear rates ( $S_{max}$ ) at the stator wall using Fluent code. A particular attention was given to the meshing of the thin gap  $\delta_{gap}$ , which has never been taken into account in previous works. This study was achieved with two cases of fluids: Newtonian and non-Newtonian shear thinning. The simulations were validated against experimental data given by Dumont [6] and Mabit et al. [11]. The analysis of shear rates field showed that the maximum shear rate is located in the clearance between the blade tip and the stator wall and that it takes an important role in SSHEs for treatment of non-Newtonian Fluids. The analysis of series of signals given by the electrochemical method [11] gave pertinent information on the prediction of the velocity profile, and the CFD model results showed the presence of a recirculation in the space between the tip of the blade and the stator wall, which creates a very complex velocity profile.

Due to floating blades, it is difficult to know the value of the gap between the tip of the blade and the stator wall, which in turn greatly influences the shear rate. The reduction of this gap between blade and stator wall gives an important increase of shear rate. However, the flow in the SSHE can be simulated for viscous Newtonian fluids by a change of gap between blade and stator wall, due to the imbalance between the viscous and centrifugal forces.

Then, a non-Newtonian fluid was used to study  $S_{max}$  with various rotating velocities. The results of the simulation gave a good agreement between the numerical and experimental results in all ranges of rotating velocities. For shear-thinning fluids, because of the low value of the viscosity, viscous forces are not important enough to oppose centrifugal forces and the position of the blades does not depend on the rotating velocity. Moreover, again for shear-thinning fluids, high shear rates are responsible for an important viscosity difference between two regions in the flow, which contributes to a higher axial flow at the wall surface.

For each type of fluids, the numerical flow behaviour close to the blade was in good agreement with experimental results. Moreover, the average shear rate in the whole computational domain corresponds to literature values.

Values of the shear rates calculated far from the blades are the only ones that do not fit experimental results precisely. In order to take into account the axial flow which has to be responsible for this difference, the presented work will be followed by a three-dimensional simulation.

The next step will be to include in the model the influence of the thermal treatment. However, temperature evolution in the exchanger takes place along the  $x$ -axis, which means that the 2D cross-section simulation will not be sufficient to handle the thermal treatment, and that the 3D analysis is first necessary.

## Appendix A. Nomenclature

$C_0$	bulk concentration ( $\text{mol m}^{-3}$ )
$d$	diameter of the microelectrode (m)
$d_h$	hydraulic diameter (m)
$d_r$	rotor diameter (m)
$d_s$	stator diameter (m)
$D$	diffusion coefficient ( $\text{m}^2 \text{s}^{-1}$ )
$e$	annular gap (m)
$F$	Faraday constant ( $\text{A s mol}^{-1}$ )
$g$	gravity acceleration ( $\text{kg m s}^{-2}$ )
$I$	limiting diffusion current (A)
$k$	consistency coefficient of the product (Oswald law ( $\text{Pa s}^n$ ))
$L$	stator length (m)
$n$	flow behaviour index of the product (Oswald law (dimensionless))
$n_l$	number of blades
$N$	rotational speed (rps = revolution per second)
$P$	pressure ( $\text{N m}^{-2}$ )
$Q$	flow rate ( $\text{m}^3 \text{s}^{-1}$ )
$R_r$	inner cylinder radius (m)
$R_s$	outer cylinder radius (m)
$Re_{ax}$	axial Reynolds number
$Re_{axg}$	generalized axial Reynolds number
$S$	local shear rate ( $\text{s}^{-1}$ )
$S_c(t)$	corrected shear rate ( $\text{s}^{-1}$ )
$S_{max}$	maximum shear rate ( $\text{s}^{-1}$ )
$t$	time (s)
$t_0$	characteristic time of the microelectrode (s)
$T$	temperature (K)
$Ta$	Taylor number
$Ta_g$	generalized Taylor number
$Ta_c$	critical values of Taylor number
$u_{ij}$	velocity component in $i$ -, $j$ -direction ( $\text{m s}^{-1}$ )
$U_d$	mean axial velocity in the annular space ( $\text{m s}^{-1}$ )
$\vec{v}$	absolute velocity vector
$\vec{v}_r$	relative velocity vector ( $\text{m s}^{-1}$ )
$z$	number of electrons

### Greek letters

$\Omega$	rotating velocity for blade and inner cylinder ( $\text{rad s}^{-1}$ )
$\delta_{gap}$	clearance between blade tip and stator wall ( $\mu\text{m}$ )
$\dot{\gamma}$	shear rate ( $\text{s}^{-1}$ )
$\eta$	dynamic viscosity (Pa s)
$\eta_0$	zero shear viscosity (cross model) (Pa s)
$\eta_\infty$	infinite shear viscosity (cross model) (Pa s)
$\eta_{min}$	minimum shear viscosity (Oswald model) (Pa s)
$\eta_{max}$	maximum shear viscosity (Oswald model) (Pa s)
$\lambda$	time constant (s)
$\theta$	circumferential coordinate (rad)
$\rho$	density ( $\text{kg m}^{-3}$ )
$\nabla$	gradient operator

## References

- [1] T.R. Bott, S. Azoory, E. Porter, Scraped surface heat exchangers. Part I. Hold-up and residence time studies, *Trans. Inst. Chem. Eng.* 46 (1968) 33–36.
- [2] M. Härröd, A literature survey of flow patterns, mixing, residence time distribution, heat transfer and power requirements, *J. Food Process Eng.* 9 (1986) 1–62.
- [3] M.B. Lakhdar, R. Cerecero, G. Alvarez, J. Guilpart, D. Flick, A. Lallemand, Heat transfer with freezing in a scraped surface heat exchanger, *Appl. Therm. Eng.* 25 (2005) 45–60.
- [4] A.M. Trommelen, W.J. Beek, Flow phenomena in a scraped-surface heat exchanger (“Votator”-type), *Chem. Eng. Sci.* 26 (1971) 1933–1942.
- [5] R. De Goede, E.J. De Jong, Heat transfer properties of a scraped-surface heat exchanger in the turbulent flow regime, *Chem. Eng. Sci.* 48 (1993) 1393–1404.
- [6] E. Dumont, Caractérisation des écoulements et des frottements pariétaux dans un échangeur de chaleur à surface raclée, Ph.D., University of Nantes, France, 1999.
- [7] J.F. Maingonnat, G. Corrieu, Etude des performances thermiques d’un échangeur de chaleur à surface raclée. 2ème partie. Influence de la dispersion axiale de chaleur sur les performances thermique, *Entropie* 111 (1983) 37–48.
- [8] J. Legrand, F. Coeuret, Transfert de matière global liquide-paroi pour des écoulements associant tourbillons de Taylor et circulation axiale forcée, *Int. J. Heat Mass Transf.* 25 (1982) 345–351.
- [9] E. Dumont, F. Fayolle, J. Legrand, Electrodiffusional wall shear rate analysis in scraped surface heat exchanger, *AIChE J.* 46 (2000) 1138–1148.
- [10] E. Dumont, F. Fayolle, J. Legrand, Flow regimes and wall shear rates determination within a scraped surface heat exchanger, *J. Food Eng.* 45 (2000) 195–207.
- [11] J. Mabit, F. Fayolle, J. Legrand, Shear rates investigation in a scraped surface heat exchanger, *Chem. Eng. Sci.* 58 (2003) 4667–4679.
- [12] M. Härröd, Methods to distinguish between laminar and vortical flow in scraped surface heat exchanger, *J. Food Process Eng.* 13 (1990) 39–57.
- [13] J.C. Leuliet, J.F. Maingonnat, G. Corrieu, Etude de la perte de charge dans un échangeur de chaleur à surface raclée traitant des produits newtoniens et non-newtoniens, *J. Food Eng.* 5 (1986) 153–176.
- [14] J.F. Maingonnat, J.C. Leuliet, T. Benezech, Modélisation de la vitesse de cisaillement apparente dans un échangeur de chaleur à surface raclée. Application aux performances thermique avec des produits non-newtoniens, *Rev. Gén. Therm.* 306–607 (1987) 381–385.
- [15] M. Naimi, Étude des lois d’écoulement et de transfert de chaleur pour des fluides non-newtoniens en espace annulaire tournant. Approche réaliste de l’échangeur à surface raclée, Ph.D., INP Lorraine, 1989.
- [16] A.M. Trommelen, W.J. Beek, H.C. Van De Westelaken, A mechanism for heat transfer in a Votator-type scraped-surface heat exchanger, *Chem. Eng. Sci.* 26 (1971) 1987–2001.
- [17] C. Skjöldebrand, T. Ohlsson, A computer simulation program for evaluation of the continuous heat treatment of particulate food products. Part 2. Utilisation, *J. Food Eng.* 20 (1993) 167–181.
- [18] M. Stranzinger, K. Feigl, E. Windhab, Non-Newtonian flow behavior in narrow annular gap reactors, *Chem. Eng. Sci.* 56 (2001) 3347–3363.
- [19] K.H. Sun, D.L. Pyle, A.D. Fitt, C.P. Please, M.J. Baines, N. Hall-Taylor, Numerical study of 2D heat transfer in a scraped surface heat exchanger, *Comput. Fluids* 33 (2004) 869–880.
- [20] W. Wang, J.H. Walton, K.L. McCarthy, Flow profiles of power law fluids in scraped surface heat exchanger geometry using MRI, *J. Food Process Eng.* 22 (1998) 11–27.
- [21] K.H. Sun, D.L. Pyle, M.J. Baines, N. Hall Taylor, A.D. Fitt, Velocity profiles and frictional pressure drop for shear thinning materials in lid-driven cavities with fully developed axial flow, *Chem. Eng. Sci.* 61 (2006) 4697–4706.
- [22] S. Patankar, *Numerical Heat Transfer and Fluid Flow*, New York, 1980.

- [23] B. Xia, D.-W. Sun, Applications of computational fluid dynamics (CFD) in the food industry: a review, *Comput. Electron. Agric.* 34 (2002) 5–24.
- [24] J. Mabit, Étude thermomécanique dans un échangeur de chaleur à surface raclée, Ph.D., University of Nantes, France, 2003.
- [25] L.P. Reiss, T.J. Hanratty, An experimental study of the unsteady nature of the viscous sublayer, *AIChE J.* 8 (1963) 154–160.
- [26] V. Sobolik, O. Wein, J. Cermak, Simultaneous measurement of film thickness and wall shear stress in wavy flow of non-Newtonian liquids, *Collect. Czech. Chem. Commun.* 52 (1987) 913–928.
- [27] F. Fayolle, J. Mabit, J. Legrand, Determination of heterogeneities in scraped surface heat exchanger using electrochemical sensors, *J. Appl. Electrochem.* 25 (2005) 487–498.